

# Cryo-SOFI enabling low-dose super-resolution correlative light and electron cryo-microscopy

Felipe Moser<sup>a,1</sup>, Vojtěch Pražák<sup>a,1</sup>, Valerie Mordhorst<sup>a,b,c</sup>, Débora M. Andrade<sup>d</sup>, Lindsay A. Baker<sup>a</sup>, Christoph Hagen<sup>a,b,c</sup>, Kay Grünewald<sup>a,b,c,e</sup>, and Rainer Kaufmann<sup>a,c,f,g,2</sup>

<sup>a</sup>Division of Structural Biology, Wellcome Trust Centre for Human Genetics, University of Oxford, OX3 7BN Oxford, United Kingdom; <sup>b</sup>Heinrich Pette Institute, Leibniz Institute for Experimental Virology, 2251 Hamburg, Germany; <sup>c</sup>Centre for Structural Systems Biology, 22607 Hamburg, Germany; <sup>d</sup>Centre for Neural Circuits and Behaviour, University of Oxford, OX1 3SR Oxford, United Kingdom; <sup>e</sup>Department of Chemistry, University of Hamburg, 20146 Hamburg, Germany; <sup>f</sup>Department of Physics, University of Hamburg, 20355 Hamburg, Germany; and <sup>g</sup>Department of Biochemistry, University of Oxford, OX1 3QU Oxford, United Kingdom

Edited by Wolfgang Baumeister, Max Planck Institute of Biochemistry, Martinsried, Germany, and approved January 28, 2019 (received for review June 21, 2018)

**Correlative light and electron cryo-microscopy (cryo-CLEM) combines information from the specific labeling of fluorescence cryo-microscopy (cryo-FM) with the high resolution in environmental context of electron cryo-microscopy (cryo-EM). Exploiting super-resolution methods for cryo-FM is advantageous, as it enables the identification of rare events within the environmental background of cryo-EM at a sensitivity and resolution beyond that of conventional methods. However, due to the need for relatively high laser intensities, current super-resolution cryo-CLEM methods require cryo-protectants or support films which can severely reduce image quality in cryo-EM and are not compatible with many samples, such as mammalian cells. Here, we introduce cryogenic super-resolution optical fluctuation imaging (cryo-SOFI), a low-dose super-resolution imaging scheme based on the SOFI principle. As cryo-SOFI does not require special sample preparation, it is fully compatible with conventional cryo-EM specimens, and importantly, it does not affect the quality of cryo-EM imaging. By applying cryo-SOFI to a variety of biological application examples, we demonstrate resolutions up to ~135 nm, an improvement of up to three times compared with conventional cryo-FM, while maintaining the specimen in a vitrified state for subsequent cryo-EM. Cryo-SOFI presents a general solution to the problem of specimen devitrification in super-resolution cryo-CLEM. It does not require a complex optical setup and can easily be implemented in any existing cryo-FM system.**

cryo-CLEM | cryo-EM | cryo-ET | fluorescence microscopy | cryogenic microscopy

**E**lectron cryo-microscopy (cryo-EM) is a powerful technique for imaging biological structures in their native environment at angstrom resolution with optimal structural preservation (1, 2). However, direct identification of specific proteins and structures in the native but crowded cellular environment remains extremely challenging. Conversely, fluorescence cryo-microscopy (cryo-FM) (3–7) excels at localization of labeled proteins but lacks higher resolving power. Therefore, correlative light and electron cryo-microscopy (cryo-CLEM; i.e., using cryo-FM to assist cryo-EM data acquisition and data interpretation) is increasingly important (8, 9). In particular, the recent introduction of super-resolution fluorescence methods for cryo-conditions (10–13) has opened up a new field of cryo-microscopy with an enormous potential for bridging the resolution gap between the two imaging modalities and for tackling a broad range of biological questions that are difficult to address with other techniques. However, it has also become clear that super-resolution cryo-FM faces many challenges, particularly the risk of specimen devitrification during super-resolution data acquisition (10, 12, 14, 15). Devitrification is the transition of amorphous ice into a crystalline form that occurs when warming up the specimen above –135 °C (16) and can lead to both damage to biological structures and loss of contrast in cryo-EM. It has become apparent that single-molecule localization microscopy under cryo-conditions (cryo-SMLM) leads to local specimen devitrification

even when applying substantially lower laser intensities than those used at ambient temperatures (10, 12). Cryo-protectants increase the temperature threshold for ice crystal formation and have been successfully used to image bacterial cells (10). However, cryo-protectants are not compatible with mammalian cells due to their adverse osmotic effects and are known to reduce contrast in cryo-EM. Formvar-coated EM grids have been explored as an alternative to carbon-coated grids due to lower light absorption, which permitted the use of higher laser intensities and therefore, a higher resolution of super-resolution cryo-FM (12). However, Formvar is highly susceptible to electron beam-induced damage, which causes bubbling and distortion of the specimen in the electron microscope and reduces the signal-to-noise ratio and image quality (12). A general solution to deal with devitrification during super-resolution imaging is currently missing, which severely hinders its applicability for cryo-CLEM.

We have developed a super-resolution cryo-FM imaging scheme that uses sufficiently low laser intensities to maintain specimens below the devitrification temperature threshold. The

## Significance

**Correlative light and electron cryo-microscopy (cryo-CLEM), the combination of fluorescence cryo-microscopy (cryo-FM) and electron cryo-microscopy, offers highly complementary information while taking advantage of optimal structural preservation through vitrification (fast crystal-free freezing) of the specimen. Introduction of super-resolution methods in cryo-FM allows for better identification and localization of rare events in noisy electron cryo-microscopy data, but high laser intensities present a challenge for maintaining the vitrified state of the specimen. Current approaches are not suitable for many potential biological applications of super-resolution cryo-CLEM. We introduce a super-resolution cryo-FM concept based on low laser intensities, which is fully compatible with electron cryo-microscopy and does not require unusual sample preparation. Due to its simplicity, it can be implemented in any existing cryo-FM system.**

Author contributions: K.G. and R.K. designed research; F.M., V.P., V.M., L.A.B., and R.K. performed research; D.M.A. contributed new reagents/analytic tools; F.M., V.P., and R.K. analyzed data; and F.M., V.P., V.M., D.M.A., L.A.B., C.H., K.G., and R.K. wrote the paper.

The authors declare no conflict of interest.

This article is a PNAS Direct Submission.

This open access article is distributed under [Creative Commons Attribution-NonCommercial-NoDerivatives License 4.0 \(CC BY-NC-ND\)](#).

Data deposition: The raw data of tomograms reported in this paper have been deposited in the EMDB (accession nos. EMD-4471–EMD4473).

<sup>1</sup>F.M. and V.P. contributed equally to this work.

<sup>2</sup>To whom correspondence should be addressed. Email: [rainer.kaufmann@cssb-hamburg.de](mailto:rainer.kaufmann@cssb-hamburg.de).

This article contains supporting information online at [www.pnas.org/lookup/suppl/doi:10.1073/pnas.1810690116/-DCSupplemental](http://www.pnas.org/lookup/suppl/doi:10.1073/pnas.1810690116/-DCSupplemental).

Published online February 26, 2019.

sample preparation method is unchanged from established cryo-EM protocols and does not influence the resolution of cryo-EM data. Our super-resolution cryo-FM image reconstruction algorithm is based on the principle of super-resolution optical fluctuation imaging (SOFI) (17), and therefore, we have termed this method cryo-SOFI. The SOFI principle makes use of fluorescence intensity fluctuations in the sample over time. When looking at the correlation of these intensity changes, only the intensity fluctuations arising from the same molecule are highly correlated, as the fluorescence of neighboring molecules (outside of the Förster resonance energy transfer regime) is independent of each other. Plotting the  $n$ th-order cumulant results in an image with a resolution improvement of up to  $n$ -fold for reweighted cross-cumulants (18) compared with a conventional image. The SOFI principle is particularly attractive for super-resolution cryo-CLEM, as fluorescence intensity fluctuations are detectable at relatively low laser intensities (17), reducing the risk of devitrification. In contrast to current super-resolution cryo-CLEM (10, 12), cryo-SOFI is not reliant on the described sample preparation workarounds and presents a general solution to the problem of devitrification in super-resolution cryo-CLEM. It can be applied to all sample types and is fully compatible with broadly used fluorescent proteins. Moreover, cryo-SOFI does not require a complex optical setup. Any cryo-FM system can be adapted easily for cryo-SOFI to enable a super-resolution cryo-CLEM workflow (*SI Appendix, Fig. S1*).

## Results

The goal of super-resolution cryo-CLEM is to combine the complementary features of cryo-FM and cryo-EM at an increased level of information content by extracting super-resolution information from the fluorescence data. To demonstrate the broad application range of cryo-SOFI in this context, we chose three different biological examples and three different fluorescent proteins as markers. Each example demonstrates that cryo-SOFI allows a clear and unambiguous correlation of cryo-FM and cryo-EM

data (Figs. 1 and 2) while maintaining the specimen in a vitrified state (*SI Appendix, Fig. S2*).

Cryo-SOFI substantially improved the confinement of fluorescent signals to areas occupied by actin in tomograms of vitrified XC cells (rat Rous sarcoma cell line, adherently grown) stably expressing Lifeact-Dendra2 (Fig. 1 *E, F, K, and L*). Pseudopodia of XC cells contained large numbers of vesicles and mitochondria in proximity to microtubule tracks reinforced by actin bundles in addition to cortical actin below the plasma membrane (*SI Appendix, Fig. S3* and *Movies S4 and S5*). The cryo-SOFI signal was concentrated to regions between the plasma membrane and intracellular vesicles, whereas the signal of conventional cryo-FM extended well outside the cellular boundary (Fig. 1 *D–F* and *J–L*). In particular, the example shown in Fig. 1*E* highlights that the labeled actin passed around two large vesicles and a mitochondrion in the region of interest (bottom right, center, and top left, respectively), whereas with conventional cryo-FM (Fig. 1*D*), the fluorescence signal overlapped with these structures. Cryo-SOFI was applied to two additional biological systems to illustrate the extra correlative power gained by improvement of the cryo-FM resolution: (*i*) XC cells transfected with the mitochondrial label mClover-TOM20 and (*ii*) COS7 cells transfected with an endoplasmic reticulum (ER)-localizing protein fused to mVenus fluorescent protein. In both cases, the structures (mitochondria or membranous/vesicular structures of the ER) observed in tomograms or micrographs match significantly better with the cryo-SOFI signal distribution, thus allowing for a better interpretation of cryo-EM data based on the information from fluorescence labeling (Fig. 2 and *SI Appendix, Fig. S4*). For example, the application of cryo-SOFI revealed that some features of similar appearance had no or very little corresponding fluorescent signal (compare structures with asterisks in Fig. 2 *G, H, K, and L* and *SI Appendix, Fig. S4 C and D*). This can be critical for choosing areas for cryo-EM data acquisition, which could otherwise not be identified with conventional cryo-CLEM.

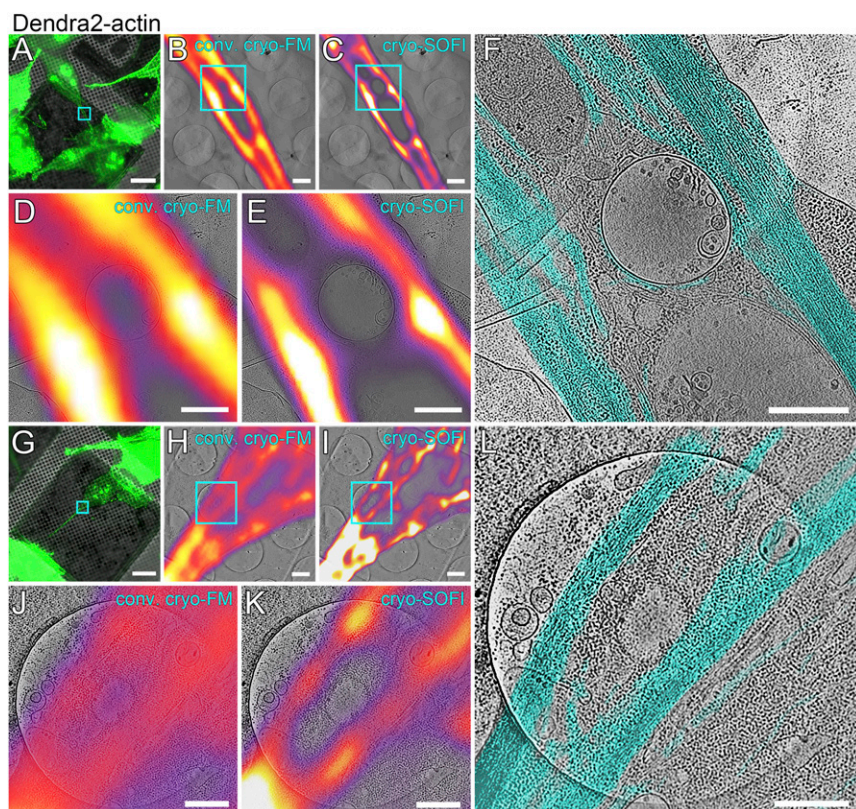
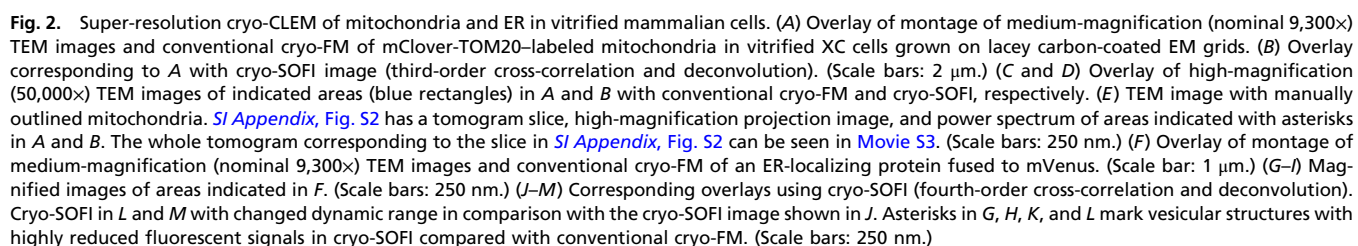


**Fig. 1.** Super-resolution cryo-CLEM of actin in vitrified mammalian cells. (*A* and *G*) Overviews of XC cells with Dendra2-Lifeact-labeled actin grown on regular patterned holey carbon foil EM grids. These images are overlays of conventional cryo-FM (green) and reflected light image (gray scale). (Scale bars: 20  $\mu$ m.) (*B* and *H*) Overlays of medium-magnification (nominal 9,300 $\times$ ) tomogram slices and conventional cryo-FM of the area indicated in *A* and *G*. (Scale bars: 1  $\mu$ m.) (*C* and *I*) Overlays corresponding to *B* and *H* with cryo-SOFI images (third-order cross-correlation and deconvolution). (Scale bars: 1  $\mu$ m.) (*D, E, J, and K*) Magnified images of the areas indicated in corresponding images in *B, C, H, and I*; *F* and *L* show sections (23-nm thickness) of corresponding tomograms overlaid with a projection of actin-containing volumes (cyan) that have been manually segmented in the whole tomograms. The 3D reconstruction of tomograms in *F* and *L* is in *Movies S1* and *S2*. (Scale bars: 500 nm.)



The preservation of the vitrified state of the specimen is perhaps the most crucial requirement for super-resolution cryo-CLEM. We have adjusted the laser intensity for cryo-SOFI data acquisition to  $\sim 100 \text{ W/cm}^2$ , a range well below previously reported super-resolution cryo-CLEM approaches [ $\sim 3$  times less than in the approach of Chang et al. (10) and  $\sim 15$  times less than the method described by Liu et al. (12)]. With an intensity of  $\sim 100 \text{ W/cm}^2$ , we see no evidence of devitrification in specimens prepared without cryo-protectants on standard EM grids with holey or lacey carbon supports (*SI Appendix, Fig. S2*). Increasing the laser intensity by only a factor of two already led to obvious ice changes in the irradiated areas and specimen damage (*SI Appendix, Fig. S5*). We restricted the laser illumination to a circular area with a diameter of  $\sim 40 \mu\text{m}$  to avoid unnecessary deposition of energy outside the field of view used for cryo-SOFI. To achieve a super-resolution image reconstruction with two- to three-times resolution improvement (resolution assessment is in *SI Appendix, Fig. S6*) over conventional cryo-FM, an acquisition time of 100 s (2,000 frames) was typically sufficient. This corresponds to 5- to 10-times time reduction compared with previously published methods (10, 12). Taken together, cryo-SOFI substantially reduces the relative photon dose deposited onto the specimen required to obtain super-resolution information and therefore, the likelihood of devitrification and specimen damage.

The SOFI method in general is very sensitive to mechanical instabilities of the setup during data acquisition (17). It was, therefore, crucial to correct for sample drift. Drift correction based on autocorrelation of bright features has been implemented into cryo-SOFI (details are in *Materials and Methods*), which allows for the correction of even relatively severe movement of the microscope stage (*SI Appendix, Fig. S7*). Data acquired with cryo-FM setups as opposed to room temperature setups are more susceptible to optical aberrations in the point spread function (PSF), mainly originating from refractive index mismatches (19). In SOFI, artifacts due to asymmetries in the PSF become more pronounced for higher-order cross-correlations (higher resolution) as the outer regions of the PSF become more relevant. Cross-correlation with repetition (20) (details are in *Materials and Methods* and *SI Appendix, Fig. S8*) minimizes the distance between correlated pixels, which decreases intensity differences and thus, diminishes aberration-related artifacts in cryo-SOFI images.

The strong background suppression and optical sectioning of the SOFI principle (17, 21) makes cryo-SOFI especially interesting for cellular samples, where it offers an even more pronounced advantage over conventional cryo-FM. Background and out-of-focus signals are eliminated during the SOFI data processing, as they exhibit minimal temporal fluctuations (17, 21). This effect is most pronounced when imaging thicker regions of the cell, where fine structural details may be missed by conventional cryo-FM due to the high out-of-focus background. Furthermore, very weak fluorescent structures also benefit from the noise suppression enabled by cryo-SOFI as shown in Fig. 3 for mVenus-labeled ER in a whole vitrified COS7 cell.

## Discussion

In summary, we have demonstrated that cryo-SOFI significantly improves the resolution of fluorescence images compared with conventional cryo-FM while maintaining vitreous specimens. In each application with cryo-SOFI, the distribution of fluorescence in the cryo-FM image is a substantially better match to the structures that are expected to contain the respective fluorescent proteins in the corresponding cryo-EM data. Cryo-SOFI allows for clear discrimination between nearby structures that would not be possible using conventional cryo-FM (Fig. 2 *F–M*). This development improves interpretation of cryo-CLEM data and simplifies correlative workflows. Furthermore, we have demonstrated the success of cryo-SOFI with three different fluorescent proteins, providing the bases for multichannel experiments. Multicolor cryo-SOFI will allow for more diverse biological experiments, expanding the scope of super-resolution cryo-CLEM.

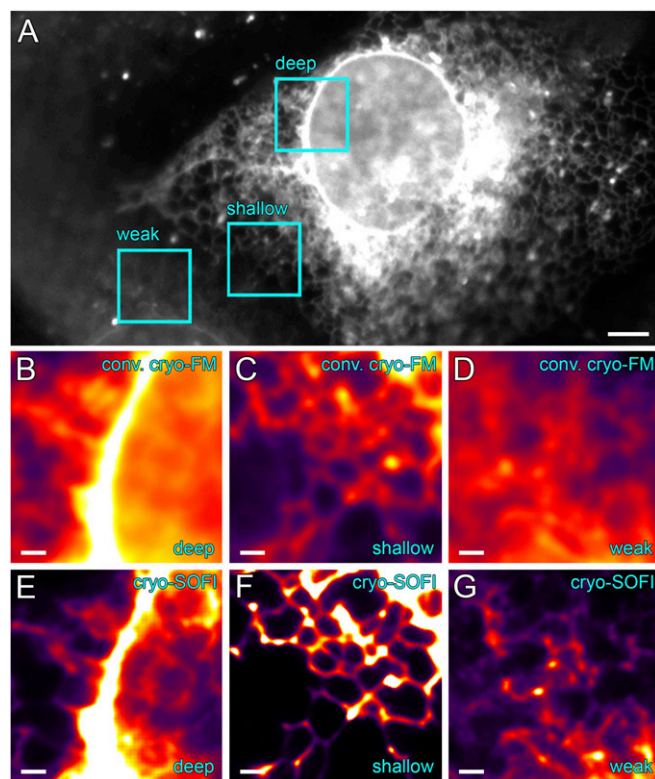


**Fig. 3.** Cryo-SOFI mVenus-labeled ER in different areas of the cell. Comparison of conventional cryo-FM (*A–D*) and cryo-SOFI (*E–G*) in areas of the cell with different optical properties: (*B* and *E*) deep = thick region around the nucleus; (*C* and *F*) shallow = thin periphery of the cell; and (*D* and *G*) weak = weakly fluorescent neighboring cell. (Scale bars: *A*, 5  $\mu\text{m}$ ; *B–G*, 1  $\mu\text{m}$ .)

We showed that cryo-SOFI, in comparison with conventional cryo-FM, is especially powerful for imaging structures in thicker parts of the cell due to its ability to suppress out-of-focus signals, thus achieving optical sectioning. In general, high background is not favorable for SOFI, but in cases where such regions inside the cell are of interest for cryo-EM, cryo-SOFI offers optical sectioning capabilities along the *z* axis comparable with a confocal microscope setup (21). Furthermore, the resolution improvement for SOFI can be extended for full 3D super-resolution imaging (17, 22). To also achieve resolution improvement along the *z* axis, time series of multiple focus planes have to be recorded simultaneously (22). This data collection scheme would require a significantly more complex optical setup than described here but would be advantageous for cryo-FM, as the relative photon dose deposited onto the specimen would remain the same. This makes cryo-SOFI particularly promising for cryo-CLEM imaging in combination with thinning methods, such as focused ion beam milling. Here, high-precision ( $\sim 100\text{-nm}$ ) localization of structures within a 3D volume is essential to reliably target regions of interest for subsequent transmission cryo-EM imaging (5).

The resolution improvement of SOFI is fundamentally not limited by diffraction (17). The sensitivity of SOFI is at the single-molecule level, as only signals of individual molecules show high temporal correlation (17). Typically, the signal-to-noise ratio of the intensity fluctuations (number of photons per single-molecule “blink” vs. background signal) is the limiting factor for resolution improvement with SOFI in biological samples (23), which also holds true for cryo-SOFI. Photobleaching is reduced by several orders of magnitude under cryo-conditions compared with ambient temperature conditions (24–26), but the combination of low fluorescence intensity in low-dose imaging, low numerical aperture (NA) of the objective lenses suitable for cryo-FM setups (14), and a high autofluorescent background in cellular samples (11, 27) limited

the resolution improvement in our system for the biological examples shown here to two to three times. We were able to successfully use cross-cumulants up to the fourth order, yielding a resolution of up to  $\sim 135$  nm (*SI Appendix, Fig. S6* has more details). For high densities of fluorescent molecules, which are typically the case in biological samples, longer acquisition times are required to recover the necessary information for higher-order SOFI reconstructions (18). For cryo-SOFI, longer acquisition times are particularly unfavorable regarding the risk of devitrification of the specimen. Higher orders would theoretically yield higher resolution but are also more prone to artifacts, as the dynamic range of a conventional wide-field image tends to get exponentially larger for SOFI reconstructions, scaling with the SOFI order being used. In addition, optical aberrations that result in an asymmetric PSF or in inconsistent PSF within the field of view as well as errors in the correction of mechanical instabilities over time affect the resulting cryo-SOFI image. The higher the order of correlation, the bigger the impact that these inconsistencies have on the resulting image. Therefore, a more stable setup, dedicated cryo-objective lenses as well as fluorophores with improved “blinking” characteristics under cryo-conditions would allow for higher orders to be used and thereby, additional improvement of the achievable resolution.

Compared with cryo-SMLM (10–12), the resolution of cryo-SOFI reaches a similar range, but the required laser intensity is severalfold lower. Liu et al. (12) demonstrated that cryo-SMLM has the potential to reach a significantly higher resolution. However, this required a special treatment of the specimen and a substrate that is not favorable for subsequent cryo-EM imaging (12).

Correction of mechanical drift in the acquired raw data is essential for cryo-SOFI. Typical artifacts of movement during data acquisition are depicted in *SI Appendix, Fig. S7*. This type of artifact can be identified by comparing the cryo-SOFI image with the conventional cryo-FM image. Additional relatively sharp features are erroneously introduced into the cryo-SOFI images along the edges of fluorescent structures in the conventional cryo-FM images. True higher-resolution features should be found within the area of the PSF of the conventional cryo-FM images (compare *SI Appendix, Fig. S7 E and H*). If drift is mainly one directional, this will also be reflected in the orientation of the artifacts and help to identify them. An active drift correction during the measurement might further improve the results of cryo-SOFI, as it has already successfully been implemented for cryo-SMLM (12). Furthermore, optical aberrations (e.g., spherical aberrations, coma) caused by refractive index mismatch (e.g., when imaging in thicker ice) or temperature changes in the objective lens (14, 15) may have detrimental effects on the quality of all super-resolution imaging techniques (28). In the case of cryo-SOFI, artifacts due to optical aberrations are typically more difficult to identify, as they are more subtle than those from mechanical instabilities (compare *SI Appendix, Figs. S7 and S8*). However, an indication of artifacts arising from optical aberrations in cryo-SOFI images is repetitive small features of the size of the SOFI PSF (*SI Appendix, Fig. S8*). Adaptive optics correction could be directly implemented in a dedicated cryo-SOFI setup in the same way as it was successfully implemented in an SMLM setup for ambient temperatures (29). This stems from the fact that both SOFI and SMLM make use of a regular wide-field microscope, in which adaptive optics correction is only necessary on the detection path. Correction of optical aberrations will become even more important with the introduction of cryo-immersion objective lenses (19) for super-resolution cryo-FM. Faoro et al. (19) recently demonstrated that small differences in temperature or refractive index of the immersion medium lead to severe aberrations of the PSF when using a cryo-immersion objective lens. Although the resolution of the described cryo-immersion objective lens with a nominal NA of 1.15 was similar to that of an 0.9 NA air objective lens under cryo-conditions, the detection efficiency was improved by a factor of 2.7 (19). The improved detection efficiency will improve the achievable resolutions of

both cryo-SOFI and other super-resolution cryo-FM approaches due to the higher photon count per single-molecule signal.

## Materials and Methods

**Sample Preparation.** XC cells (provided by Quentin Sattentau, University of Oxford, Oxford, United Kingdom) and COS7 cells were propagated in Gibco DMEM GlutaMAX (Thermo Fisher) with 10% FCS at 37 °C and 5% CO<sub>2</sub>. To generate stable cell lines expressing Dendra2-Lifeact, XC cells were transfected with pDendra2-Lifeact-7 [pDendra2-Lifeact-7 was a gift from Michael Davidson, Florida State University, Tallahassee, FL (Addgene plasmid 54694)] using X-tremeGENE HP DNA Transfection Reagent (Sigma) and selected with G-418 (Sigma). Cells used for this study tended to avoid growing over holes in the carbon support film of EM grids and instead, clustered to the metal bars; only a small number of cells could be imaged in cryo-EM as a result. To deal with this issue, graphene oxide (GO) sheets were deposited on EM grids to form a continuous surface and a better substrate for cell adhesion using a method based on the work by Bokori-Brown et al. (30). Multilayer GO sheets are fluorescent, but these can be removed by centrifugation, and we did not observe a substantial increase of background fluorescence on GO-coated grids compared with conventional grids. Glow-discharged gold finder grids (Quantifoil) were incubated with GO solution, washed with water, and allowed to dry. However, we found that GO detached from the carbon support during coating with cell adhesion material and subsequent cell culture. To prevent this, GO was cross-linked to the carbon support using 4% paraformaldehyde, washed with water, and coated with 50 mg/mL fibronectin in PBS. Cells were grown on coated grids for 24 h before plunge freezing. XC cells were transfected with a plasmid containing mClover-TOM20 [mClover-TOM20-N-10 was a gift from Michael Davidson (Addgene plasmid 56307) (31)] and grown on gold finder grids with single-layer GO on lacey carbon support (EM Resolutions) coated with fibronectin. To obtain COS7 cells with mVenus-marked ER, cells were transfected using Lipofectamine 2000 (Thermo Fisher) with a plasmid (provided by Elena Seiradake, University of Oxford, Oxford, United Kingdom), which consists of the transmembrane helix of the human RPTPmu fused to mVenus. Transfected cells were detached by trypsin and seeded onto carbon-coated grids (Quantifoil), and then, they were grown for 24 h before freezing.

**Cryo-SOFI Setup and Data Acquisition.** We modified a commercial cryo-FM system (Cryo CLEM; Leica) equipped with a 50 $\times$  0.9-NA objective lens (Cryo CLEM Objective HCX PL APO 50 $\times$ 0.9; Leica) for cryo-SOFI imaging by coupling lasers (iChrome MLE; Toptica) into the microscope body for fluorophore excitation and photoswitching. Laser light after the single-mode fiber was collimated using an achromatic lens with 19-mm focal length to achieve an illuminated area of  $\sim 40$ - $\mu$ m diameter in the object plane. A schematic illustration of additionally required hardware is in *SI Appendix, Fig. S1*. For all biological examples presented here, data were acquired using 488-nm laser illumination and the standard GFP filter cube of the microscope system (excitation: 470/40; dichroic: 495 low pass; emission: 525/50). Overview images were recorded using a standard CCD camera (DFC365 FX; Leica). Cryo-SOFI data were recorded with an electron multiplying CCD (EMCCD) camera (iXon Ultra 897; Andor) and additional 2 $\times$  magnification to reach an overall magnification of 100 $\times$  for matching the larger pixel size of the EMCCD camera. Typical camera settings for cryo-SOFI data acquisition were 50-ms integration time per frame (at a rate of 20 frames per second) for a time series of 2,000 images at an EM gain of 20–200.

**Cryo-SOFI Drift Correction and Image Reconstruction.** Drift and other mechanical instabilities were determined using an autocorrelation-based approach. Bright structures in the specimen or added fiducial markers were used as reference objects. Whichever signal is used for the drift correction, it is important to have a very high density of fluorescent molecules to prevent errors in the estimation of the drift due to intensity fluctuations. Every image in the data stack was compared with the first one using the findshift routine of the DIPImage toolbox ([diplib.org](http://diplib.org)) for MATLAB (Mathworks). Typically (depending on the pixel size of the raw data) for the SOFI principle, it is important to determine the drift of the sample with subpixel accuracy. The obtained lateral shifts for each image in the raw data stack are then used to correct the drift during data acquisition.

Cryo-SOFI image reconstruction on the drift-corrected data has been performed as described previously for ambient temperature SOFI (17, 18). For cryo-SOFI, where aberrations in the PSF can be more severe, close attention had to be paid to the effects of asymmetries in the PSF on the cross-correlation SOFI images. In comparison with autocorrelation SOFI, which is based on (and restrained to) the actual physical pixels on the camera,

cross-correlation SOFI ( $XC_n$ ) makes use of virtual pixels in between the physical pixels in the raw images:

$$XC_n(\vec{r}_1, \dots, \vec{r}_n, \tau_1, \dots, \tau_n) = \prod_{j=1}^n U\left(\frac{\vec{r}_j - \vec{r}_1}{\sqrt{n}}\right) \cdot \sum_{i=1}^N U^n\left(\vec{r}_i - \frac{\sum_{k=1}^n \vec{r}_k}{\sqrt{n}}\right) \cdot \epsilon_i^n \cdot \omega_i(\tau_1, \dots, \tau_n), \quad [1]$$

with  $\vec{r}$  being the position of the correlated pixels,  $U$  being the PSF of the original images,  $\omega$  being the temporal weighting factor, and  $\tau$  being the time delays between each pixel (17). The PSF function in Eq. 1 implies that calculated pixel position  $\vec{r}$  is at the geometrical center of the correlated pixel. It also shows that each pixel in the SOFI image is dependent on a pixel distance

correction factor  $U\left(\frac{\vec{r}_1 - \vec{r}_2}{\sqrt{n}}\right)$ , which corrects for the difference in intensity due to the difference in distance from the correlated pixel (18). This pixel correction factor is very susceptible to optical aberrations in the system. Cross-correlation SOFI images can be calculated in two different ways (20). One uses only different pixels (cross-correlation without repetition). This results in a higher amount of information used to calculate the SOFI pixel value (20), in larger distances between the correlated pixels, and thus, in a higher probability of aberrations affecting the resulting super-resolution image. That happens, because a PSF formed in the presence of optical aberrations has an FWHM isosurface larger than that of an optimal PSF (28). By using different pixels but allowing some of them to be repeated, a cross-correlation with repetition is obtained (20). This minimizes the distance between correlated pixels to minimize the effects of aberrations in the PSF (details and an example are in *SI Appendix, Fig. S8*). The pixel distance corrections were calculated by comparing a second-order autocorrelation image with an image calculated with a second-order cross-correlation. The difference between them is the pixel distance correction factor:  $U\left(\frac{\vec{r}_1 - \vec{r}_2}{2}\right)$ , with the positions  $\vec{r}_1$  and  $\vec{r}_2$  of the pixels at either side of the autocorrelated pixel.

The PSF used for the deconvolution was obtained by dividing the SOFI image by one of the according images of one order lower (compare Eq. 1 for order  $n$  and  $n - 1$ ). In this manner, the actual PSF was directly obtained from each experiment. This minimizes artifacts typical for deconvolution due to the application of an inaccurate PSF. For all biological examples shown here,

cross-correlation SOFI up to the third or fourth order yielded good super-resolution images. Combined with deconvolution, this resulted in a resolution improvement of approximately two to three times. MATLAB code for cryo-SOFI image reconstruction can be downloaded via the following link: <https://github.com/rainerkaufmann/cryoSOFI/releases>.

**Cryo-EM Imaging.** Micrographs were collected on a Tecnai F30 “Polara” (FEI) operating at 300 keV with a postcolumn QUANTUM 964 energy filter (Gatan) operated in Zero-Loss mode using a 20-eV energy slit and K2 Summit direct electron detector (Gatan) operating in counting mode at 2.84-, 4.22-, or 23.1-Å pixel size. A 70-μm C2 aperture was used during all data acquisition. Where possible, tilt series were collected bidirectionally from −55° to 59° at 3° increments with 10 frames per image. Frames were aligned using Unblur (32), and tomograms were reconstructed using IMOD Etomo (33). Tomograms were binned two or eight times and bandpass filtered for visualization using Bsoft (34). Raw tomograms of images shown in Fig. 1 D–F and J–L and *SI Appendix, Figs. S2B and S3 B and C* have been deposited as EMD-4471–4473 in the EMDDB.

**Overlay of Cryo-FM and Cryo-EM Images.** Overlays of cryo-FM (conventional and cryo-SOFI) and cryo-EM images were performed by identifying distinct features visible in both imaging modalities and marking their positions using the Control Point Selection Tool of MATLAB (Mathworks). These positions allowed us to determine the transformation between the different coordinate systems. For the biological samples presented here, sufficient structural similarities between cryo-FM and cryo-EM images could be identified for the correlation. In other cases, fiducial markers visible in cryo-FM and cryo-EM can be used for the determination of the coordinate transformation and overlay of the images (35, 36).

**ACKNOWLEDGMENTS.** We thank E. Yvonne Jones, Jordan Raff, Ilan Davis, and Ian M. Dobbie for fruitful discussions and continuous encouragement. We acknowledge support from Cancer Research UK Grant A17721, Canadian Institute of Health Research Fellowship 339062 (to L.A.B.), Wellcome Trust Grants 107806/Z/15/Z (to K.G.) and 107457/Z/15/Z (to Micron Oxford), Human Frontier Science Program Grant RGP 0055/2015 (to K.G.), and Volkswagen Foundation Freigeist Fellowship 91671 (to R.K.).

- Glaeser RM (2016) How good can cryo-EM become? *Nat Methods* 13:28–32.
- Orlov I, et al. (2017) The integrative role of cryo electron microscopy in molecular and cellular structural biology. *Biol Cell* 109:81–93.
- Swulius MT, et al. (2011) Long helical filaments are not seen encircling cells in electron cryotomograms of rod-shaped bacteria. *Biochem Biophys Res Commun* 407:650–655.
- Strnad M, et al. (2015) Correlative cryo-fluorescence and cryo-scanning electron microscopy as a straightforward tool to study host-pathogen interactions. *Sci Rep* 5:18029.
- Arnold J, et al. (2016) Site-specific cryo-focused ion beam sample preparation guided by 3D correlative microscopy. *Biophys J* 110:860–869.
- Hampton CM, et al. (2017) Correlated fluorescence microscopy and cryo-electron tomography of virus-infected or transfected mammalian cells. *Nat Protoc* 12:150–167.
- Ader NR, Kukulski W (2017) triCLEM: Combining high-precision, room temperature CLEM with cryo-fluorescence microscopy to identify very rare events. *Methods Cell Biol* 140:303–320.
- Hauser M, et al. (2017) Correlative super-resolution microscopy: New dimensions and new opportunities. *Chem Rev* 117:7428–7456.
- Schorb M, et al. (2017) New hardware and workflows for semi-automated correlative cryo-fluorescence and cryo-electron microscopy/tomography. *J Struct Biol* 197:83–93.
- Chang YW, et al. (2014) Correlated cryogenic photoactivated localization microscopy and cryo-electron tomography. *Nat Methods* 11:737–739.
- Kaufmann R, et al. (2014) Super-resolution microscopy using standard fluorescent proteins in intact cells under cryo-conditions. *Nano Lett* 14:4171–4175.
- Liu B, et al. (2015) Three-dimensional super-resolution protein localization correlated with vitrified cellular context. *Sci Rep* 5:13017.
- Nahmani M, Lanahan C, DeRosier D, Turrigiano GG (2017) High-numerical-aperture cryogenic light microscopy for increased precision of superresolution reconstructions. *Proc Natl Acad Sci USA* 114:3832–3836.
- Wolff G, Hagen C, Grünwald K, Kaufmann R (2016) Towards correlative super-resolution fluorescence and electron cryo-microscopy. *Biol Cell* 108:245–258.
- Bykov YS, Cortese M, Briggs JAG, Bartschschlager R (2016) Correlative light and electron microscopy methods for the study of virus-cell interactions. *FEBS Lett* 590:1877–1895.
- Dubochet J (2007) The physics of rapid cooling and its implications for cryoimmobilization of cells. *Methods Cell Biol* 79:7–21.
- Dertinger T, Colyer R, Iyer G, Weiss S, Enderlein J (2009) Fast, background-free, 3D super-resolution optical fluctuation imaging (SOFI). *Proc Natl Acad Sci USA* 106:22287–22292.
- Dertinger T, Colyer R, Vogel R, Enderlein J, Weiss S (2010) Achieving increased resolution and more pixels with superresolution optical fluctuation imaging (SOFI). *Opt Express* 18:18875–18885.
- Faoro R, et al. (2018) Aberration-corrected cryoimmersion light microscopy. *Proc Natl Acad Sci USA* 115:1204–1209.
- Geissbuehler S, et al. (2012) Mapping molecular statistics with balanced super-resolution optical fluctuation imaging (bSOFI). *Opt Nanoscopy* 1:4.
- Dertinger T, Xu J, Naini OF, Vogel R, Weiss S (2012) SOFI-based 3D superresolution sectioning with a widefield microscope. *Opt Nanoscopy* 1:2.
- Geissbuehler S, et al. (2014) Live-cell multiplane three-dimensional super-resolution optical fluctuation imaging. *Nat Commun* 5:5830.
- Dertinger T, et al. (2013) Advances in superresolution optical fluctuation imaging (SOFI). *Q Rev Biophys* 46:210–221.
- Moerner WE, Orrit M (1999) Illuminating single molecules in condensed matter. *Science* 283:1670–1676.
- Sartori A, et al. (2007) Correlative microscopy: Bridging the gap between fluorescence light microscopy and cryo-electron tomography. *J Struct Biol* 160:135–145.
- Schwartz CL, Sarbash VI, Ataullakhanov FI, McIntosh JR, Nicastro D (2007) Cryo-fluorescence microscopy facilitates correlations between light and cryo-electron microscopy and reduces the rate of photobleaching. *J Microsc* 227:98–109.
- Carter SD, et al. (2018) Distinguishing signal from autofluorescence in cryogenic correlated light and electron microscopy of mammalian cells. *J Struct Biol* 201:15–25.
- Booth M, Andrade D, Burke D, Patton B, Zurauskas M (2015) Aberrations and adaptive optics in super-resolution microscopy. *Microscopy (Oxf)* 64:251–261.
- Burke D, Patton B, Huang F, Bewersdorf J, Booth MJ (2015) Adaptive optics correction of specimen-induced aberrations in single-molecule switching microscopy. *Optica* 2:177–185.
- Bokori-Brown M, et al. (2016) Cryo-EM structure of lysenin pore elucidates membrane insertion by an aerolysin family protein. *Nat Commun* 7:11293.
- Lam AJ, et al. (2012) Improving FRET dynamic range with bright green and red fluorescent proteins. *Nat Methods* 9:1005–1012.
- Grant T, Grigorieff N (2015) Measuring the optimal exposure for single particle cryo-EM using a 2.6 Å reconstruction of rotavirus VP6. *eLife* 4:e06980.
- Kremer JR, Mastronarde DN, McIntosh JR (1996) Computer visualization of three-dimensional image data using IMOD. *J Struct Biol* 116:71–76.
- Heymann JB (2001) Bsoft: Image and molecular processing in electron microscopy. *J Struct Biol* 133:156–169.
- Schellenberger P, et al. (2014) High-precision correlative fluorescence and electron cryo microscopy using two independent alignment markers. *Ultramicroscopy* 143:41–51.
- Schorb M, Briggs JA (2014) Correlated cryo-fluorescence and cryo-electron microscopy with high spatial precision and improved sensitivity. *Ultramicroscopy* 143:24–32.